A new general purpose event horizon finder for 3D numerical spacetimes

Peter Diener

Max-Planck-Institut für Gravitationsphysik, Albert-Einstein-Institut, Am Mühlenberg 1, D-14476 Golm, Germany

E-mail: diener@aei.mpg.de

Abstract. I present a new general purpose event horizon finder for full 3D numerical spacetimes. It works by evolving a complete null surface backwards in time. The null surface is described as the zero level set of a scalar function, that in principle is defined everywhere. This description of the surface allows the surface, trivially, to change topology, making this event horizon finder able to handle numerical spacetimes, where two (or more) black holes merge into a single final black hole.

PACS numbers: 04.25.Dm, 04.70.Bw, 95.30.Sf, 97.60.Lf

Submitted to: *Class. Quantum Grav.*

1. Introduction

An event horizon (EH) is defined as a 2+1 surface in 3+1 space, inside of which no null geodesics can reach future null infinity, while outside at least some can. For that reason an EH is a global concept and can in principle only be found when the full history of the spacetime is known. The horizon itself is generated by outgoing null geodesics, that once they have joined onto the horizon will forever stay on it.

In recent years 3D numerical evolutions of binary black hole spacetimes have become stable enough that it is possible in some cases to follow the final merged black hole for a significant time [1]. Therefore it makes sense to start looking for EHs in these numerical spacetimes. However, previously published EH finders for numerical spacetimes [2, 3, 4, 5] have either been too slow, limited to single black hole spacetimes or have taken advantage of special symmetries in order to handle changes in topology and can not be used in the general 3D case without symmetries.

This paper is organized in the following way. In section 2 I will present the basic ideas and methods of EH finding. In section 3 I will discuss different ways of describing the surface and present the level set description used here. The numerical implementation is described in section 4, where also a cure for a very serious problem is presented. In section 5 I will present tests of the EH finder using analytical data with known location of the EH to test the accuracy of the code while in section 6 I will present tests using numerical data in order to test the robustness of the code. Finally in section 7 I will discuss prospects of future work and uses of the code.

2. Event horizon finding

In principle the EH can be found by integrating null geodesics forward in time. Outgoing null geodesics just outside or inside the EH will all diverge away from the EH. Those outside will escape to infinity, while those inside will end up at the singularity. However, as pointed out in [4] it is practically impossible to follow the generators of the horizon forward in time, since small numerical errors will cause the null geodesics to deviate exponentially away from the EH. This can, on the other hand, be taken advantage of, if the generators are integrated backwards in time, since then the EH will be an attractor. A method based on this was presented in [3].

For the backward null geodesic integration method, the presence of a small tangential velocity component can cause the null geodesics to deviate from the EH. Even though the null geodesic may return to the EH, it will be in a different position and it might even cross other null geodesics, thereby creating spurious caustics. The cure is to evolve the complete horizon surface as a whole. Since the only way a surface can move is in its normal direction, tangential drift is not an issue. This can be done by representing the surface by a function

$$f(t, x^i) = 0, \tag{1}$$

and requiring this surface to satisfy the null condition

$$g^{\alpha\beta}\partial_\alpha f \partial_\beta f = 0. \tag{2}$$

Expanding equation (2) out yields a quadratic equation for $\partial_t f$, which can be solved, giving the following evolution equation for f

$$\partial_t f = \frac{-g^{ti}\partial_i f + \sqrt{(g^{ti}\partial_i f)^2 - g^{tt}g^{ij}\partial_i f \partial_j f}}{g^{tt}}. \tag{3}$$

Here the root was chosen so as to describe outgoing null geodesics. Notice that, in contrast to the geodesic equation, this equation does not contain any derivatives of the metric.

Note that the exact location of the EH is unknown at the end of a numerical evolution. However the location of the apparent horizon (AH) can serve as a good initial guess for the EH (see [6, 7, 8, 9, 10, 11, 12, 13, 14, 15, 16, 17] for details about finding AHs). It will be completely inside the EH, but will be very close if the numerical spacetime is almost stationary. A practical way of locating the EH is to start with the AH as an initial guess for the EH and to use the attracting property of the EH to approach it asymptotically. It is therefore important to note that the surface $f = 0$ will never exactly coincide with the EH, but will approach it exponentially. In order to estimate when the surface $f = 0$ is a good approximation, a different initial surface (chosen so as to be completely outside of the EH) can be evolved backwards in time. The EH will then always be located between these two surfaces and when the two surfaces agree to within a small fraction of a grid cell the location of the EH is known with sufficient accuracy.

3. Description of the surface

In [4] either of the following parametrization was adopted to describe the surface in the presented axisymmetric cases

$$f(t, r, \theta) = r - s(t, \theta), \qquad (4)$$

$$f(t, z, \rho) = \rho - s(t, z), \qquad (5)$$

where equation (5) was used in the colliding black hole case, in order to allow the surface to cross itself thereby describing the locus of generators before they join onto the EH. This was possible due to the high level of symmetry, but would be difficult to generalize to the non symmetric case, since it requires prior knowledge of the location of the caustic points (in this case the symmetry axis).

The choice made in this work, is to avoid any parametrization of the surface that might run into trouble, but to keep the description in equation (1). That is, the horizon surface is described as the 0-level isosurface of the scalar function f, where f is negative inside and positive outside the surface. There are several advantages to this choice. The main advantage is that changes of topology (such as when black holes merge) are handled naturally with no special symmetry requirements. What happens in these cases is simply that the number of regions with negative f-values changes. Another advantage is that the function f is defined at the same grid points as the numerical metric so that no interpolation is necessary in order to evolve the surface. The last point can also be seen as a disadvantage, since when f is defined on fixed grid points only, there are in general no grid points exactly on the $f = 0$ isosurface. This means that in order to analyze the surface it is necessary to find it first. A second (and more serious) problem is the fact that during evolution of f its gradients steepen. This can be seen in the following way: The level set function f actually defines an infinity of surfaces with different iso-values. Thus for example the triplet of iso-values $f = [-0.5, 0.0, 0.5]$ defines three outgoing null surfaces that will all move towards the EH, when evolved backwards in time. This means that these three surfaces will move towards each other and since they are defined by constant values of f, the gradients will steepen. This will cause numerical problems if it is not addressed. Another potential problem is illustrated in Appendix A, where it is shown that for at least one choice of the metric (Schwarzschild in Kerr-Schild coordinates), the evolution of f is ill conditioned.

4. Numerics

The evolution of equation (3) is performed using the Method of Lines (MoL) with either second order Runge-Kutta (RK2) or 3-step Iterative Crank Nicholson (ICN). The spatial derivatives of f are calculated using one sided second order derivatives. The directions of the derivatives are determined by different schemes depending on the problem. If the shift is zero, the directions are determined using the values of f itself according to the scheme in Appendix B. On the other hand if the shift is non-zero, the direction of the shift has to be taken into account in order to preserve stability, the main reason being that the evolution equation contains terms of the form $g^{ti}\partial_i f$. In this case the stencil direction is taken to be opposite the shift direction, since I am evolving backwards in time.

In order to be able to handle numerical data with excised regions, the code supports dynamic interior excision regions, that can be used even when the numerical data is defined everywhere. Since the EH normally does not occupy the whole numerical domain it is only necessary to output a rectangular box that contains the EH at all times. This can result in a very significant reduction of the amount of required disk space for the numerical metric data. Furthermore to save computation time, once the numerical data has been read in, the computationally active region can be further reduced so that only a smaller rectangular box surrounding the black holes is used. As the holes move across the grid, this smaller active region moves along with them by de-activating and activating grid points as necessary. At the interior boundaries and the boundaries of the rectangular box, one sided second order derivatives are used as well.

The initial guess for f at $t = T$, where T is the time at the end of the numerical evolution, is normally chosen as a sphere of radius r_0 centered at the point $P = (x_0, y_0, z_0)$

$$f(T, x, y, z) = \sqrt{(x - x_0)^2 + (y - y_0)^2 + (z - z_0)^2} - r_0, \tag{6}$$

which has the nice property that

$$|\nabla f| = 1, \tag{7}$$

except at the origin where it is non differentiable. The parameters for the initial guess are chosen to be as good a guess for the EH as possible, while making sure that $f = 0$ is either completely inside or outside of the EH. If the EH is judged (for example by looking at the shape of the AH) to be significantly nonspherical it is also possible to use an arbitrarily oriented and shaped ellipsoid as the initial guess. This has not been necessary so far since, with the currently used gauge conditions, the final horizon is almost always close to being a coordinate sphere.

As mentioned, there is a problem with gradients of f steepening during the evolution. For that reason f is re-initialized regularly during the evolution so that it again satisfies equation (7) approximately. To obtain this re-initialization the evolution equation

$$\frac{\mathrm{d}f}{\mathrm{d}\lambda} = -\frac{f}{\sqrt{f^2 + 1}} \left(|\nabla f| - 1\right) \tag{8}$$

is evolved in an unphysical parameter λ until a steady state has been achieved. The factor in front of the parenthesis in equation (8) consists of two parts. The numerator is present to make sure that no evolution takes place when $f = 0$, since I do not want to move the surface during re-initialization. The denominator is there to make sure that the Courant condition for stability is limited by the constant value, 1, instead of the maximum value of f. The term in the parenthesis makes sure that the evolution stops when $|\nabla f| = 1$. The evolution of equation (8) is also done with MoL, but since it is only the final steady state that are significant, it is sufficient to use a simple Euler scheme. However, a second order Runge-Kutta scheme has been implemented as well. The spatial derivatives used for the re-initialization are second order upwinded according to the scheme in Appendix B. Since the re-initialization equation does not depend on the shift, the shift direction is ignored.

If the re-initialization is performed often enough, I do not have to worry about potential stability problems due to the use of one sided differences of f at the boundaries. This is the main reason, that it is possible to evolve only a small region around the $f = 0$ surface. Note also, that without re-initialization all different $f = const$ surfaces would be evolved as null surfaces, but every time re-initialization is done all surfaces except $f = 0$ will be changed, so they can not any more be considered to be null surfaces. In this way $f = 0$ is picked out as the surface of interest.

The re-initialization equation (8) is similar to the one used in [18], the differences being introduced to make the surface move as little as possible, while still being reasonably fast.

This re-initialization scheme works well most of the time, but it has some problems when there is only a few points in either directions inside the surface. In those circumstances the level 0 isosurface can move significantly outwards. This typically occurs just before the topology of the surface changes. To avoid this, a scheme has been implemented to detect when this happens and avoid doing the re-initialization until after the topology has changed. The detection scheme essentially consists of searching for all places where 1) f is negative (i.e. inside the surfaces) and 2) there is a local extremum of f in all directions. Since the value of f in such a grid point is approximately equal to the signed distance from that grid point to the level 0 isosurface, the absolute value of the maximum of f in these points can be used to estimate the minimum width of the region with $f < 0$. If this width is less than a given threshold, the re-initialization is not done.

In order to calculate the areas of the EHs, it is necessary to locate points on the surfaces. This task is complicated by the fact that in principle, the number of individual surfaces at any given time is not known. Therefore points on the surfaces present are located in several separate steps.

First the number of surfaces in the data is found. This is done using a “flooding” algorithm using an integer mask (`surface_mask`) initialized to zero at the grid points of the level set function, f, and an integer counter (`surface_counter`) initialized to zero. The algorithm proceeds as follows. Locate a grid point where $f < 0$ and `surface_mask=0`. If such a grid point does not exist there are no surfaces, so exit. Otherwise increment `surface_counter` and mark this point `surface_mask=surface_counter`. Repeatedly find connected grid points inside the same surface, i.e. locate points with $f < 0$ and at least one neighbour point with `surface_mask=surface_counter` and mark those likewise until no more such points can be found. In this way all points inside the first surface has been marked. Now check if another point with $f < 0$ and `surface_mask=0` exists. This point must then be located inside another surface. Repeat the above marking procedure until all points with $f < 0$ has been marked with a surface number.

Next an approximate coordinate centroid is found for each surface using the marked points. This is used as the center for a polar coordinate system used to explicitly parametrize the corresponding surface as $r(\theta, \phi)$. For each chosen direction (given by θ and ϕ) the radius of the surface is found using interpolated values of f in a Newton iteration root finder‡.

With this explicit parametrization of the surface, the area, centroid and circumferences can be easily computed. Unfortunately it is not always possible to find this explicit parametrization. As shown later in Section 6.2 the EH can in some cases be so distorted that with any choice of center, f would be multivalued along some angular directions. For this reason a more general surface finding and integration routine using a direct triangulation of the surfaces is under consideration.

I would like to emphasize that the use of interpolation is only necessary when finding points on the surfaces for analysis purposes and is not used at all in the evolution and re-initialization of the level set function.

The EH finding algorithm has been implemented as a thorn in Cactus [19, 20] using the Einstein Toolkit [21] and is fully parallelized. Though it might happen that the computationally active region is contained completely on one processor, this is usually not a serious concern since the thorn uses a lot less memory than a comparably sized numerical evolution and can therefore be run on a lot less processors. Also it is not necessary to run the EH finder on the full computational grid of the spacetime evolution. It suffices to output just the part of the grid that completely contains the EH (or horizons) within it at all times, also cutting down on the required disk space for output.

The source code for the EH finder, will be released for public use in the near future.

5. Tests using analytical data

In this section I will present tests of the code using analytic spacetimes, where the location of the EH is known analytically at all times.

‡ A Hermite interpolation polynomial is used, since not only the function but also the derivative has to be continuous in the Newton iteration.

5.1. Non-rotating black hole in isotropic coordinates

The first test uses the metric for a non-rotating black hole in isotropic coordinates. In these coordinates the metric is

$$\mathrm{d}s^2 = -\left(\frac{1-M/(2r)}{1+M/(2r)}\right)^2 \mathrm{d}t^2 + \left(1+\frac{M}{2r}\right)^4 [\mathrm{d}r^2 + r^2(\mathrm{d}\theta^2 + \sin^2\theta \mathrm{d}\phi^2)],$$

where M is the mass of the black hole. In these coordinates the horizon is a stationary sphere with radius $r_{EH} = M/2$. The equation of motion for radial outgoing null geodesics is

$$\frac{\mathrm{d}r}{\mathrm{d}t} = \frac{1-M/(2r)}{(1+M/(2r))^3}.$$

Looking at null geodesics close to the EH $r = M/2+\epsilon$ where $\epsilon << M/2$ and expanding it can be seen that

$$\frac{\mathrm{d}\epsilon}{\mathrm{d}t} \approx \frac{\epsilon}{4M}.$$

So integrating forward in time the null geodesic diverges exponentially from the EH. However integrating backwards in time it should be expected that the null surface converges exponentially to the location of the EH with an e-folding time of $4M$.

I performed runs at three different resolutions $\Delta = 0.05M, 0.025M, 0.0125M$ for $M = 1$ with an initial radius for the null surface equal to $r_0 = 0.4M$ (i.e. 2, 4 and 8 gridspacings away from the true EH). In figure 1 I show the maximum distance of the surface from the true location of the EH divided by the gridspacing as a function of time in a logarithmic plot. Initially there is a clear exponential convergence until the finite difference solution is reached with a numerical e-folding time of $4.13M$, agreeing nicely with the analytic expectation. At higher resolution the finite difference solution is closer to the analytic solution. At a resolution of $\Delta = 0.05$ the maximum error at $T = -100M$ is 0.0097Δ. At the higher resolution of $\Delta = 0.025$ the corresponding error is 0.0056Δ,and at the highest resolution of $\Delta = 0.0125M$ the error is 0.0031Δ. Looking at the ratio of the error at successive resolutions, it can be seen that the code is approaching second order convergence. Looking at the absolute errors it is worth noting that the method is able to locate the EH to less than 1/100 of a grid spacing when the radius of the EH is only 10 grid spacings.

5.2. Non-rotating black hole in Kerr-Schild coordinates

The second test uses the metric for a non-rotating black hole in Kerr-Schild coordinates. In these coordinates the metric is

$$\mathrm{d}s^2 = \left(-1+\frac{2M}{r}\right)\mathrm{d}t^2 + \frac{4M}{r}\mathrm{d}t\mathrm{d}r + \left(1+\frac{2M}{r}\right)\mathrm{d}r^2 + r^2(\mathrm{d}\theta^2 + \sin^2\theta \mathrm{d}\phi^2). \quad (9)$$

Just like in the previous section it is easy to find the equation of motion for radial outgoing null geodesics and analyse the limit of null geodesics, close to the EH (in these coordinates $r_{EH} = 2M$). The result is that the e-folding time is $4M$ for these coordinates as well.

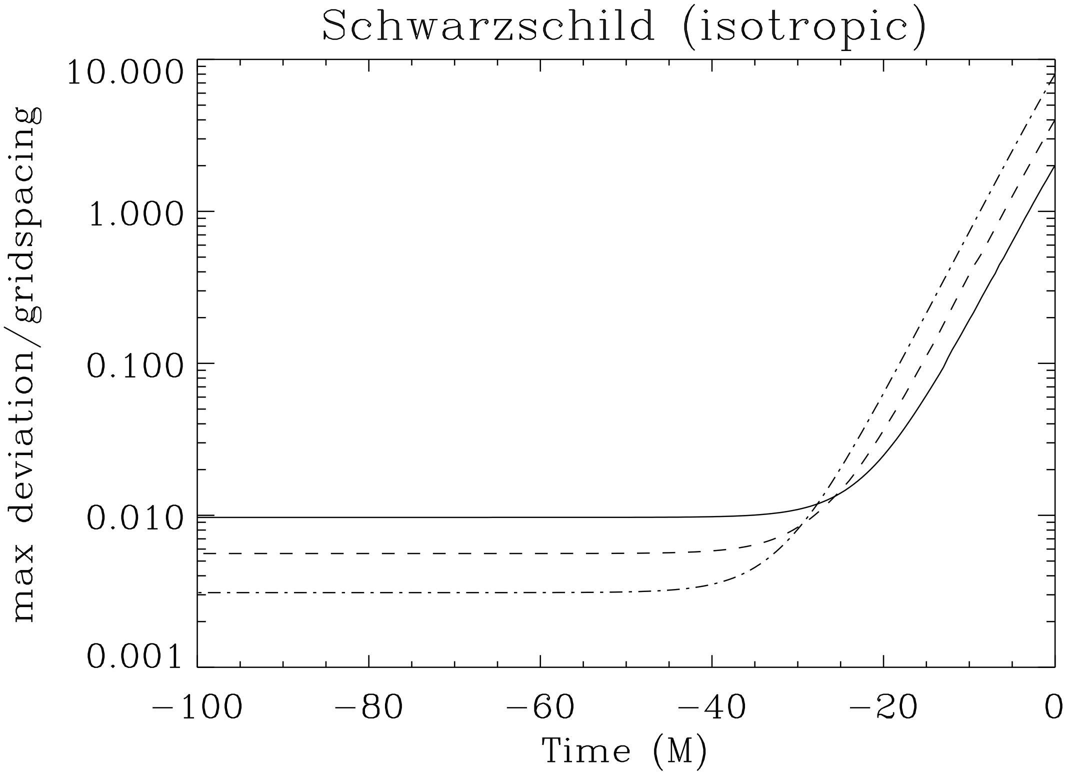

Figure 1. The maximum deviation of the surface from the analytic EH divided by the gridspacing for a Schwarzschild black hole of mass $M = 1$ in isotropic coordinates as function of time. The solid line is $\Delta = 0.05M$, the dashed line is $\Delta = 0.025M$ and the dash-dot line is $\Delta = 0.0125M$.

Here I performed runs at three different resolutions $\Delta = 0.2M, 0.1M, 0.05M$ for $M = 1$ with an initial radius for the null surface equal to $r_0 = 1.8M$ (i.e. 2, 4 and 8 gridspacings away from the true EH). In figure 2 I show the maximum distance of the surface from the true location of the EH divided by the gridspacing as a function of time in a logarithmic plot. Again there is a clear exponential convergence until the finite difference solution is reached with a numerical e-folding time of 4.01 in excellent agreement with the analytic expectation. Also in this case, the higher the resolution the closer the finite difference solution is to the analytic solution. The maximal error divided by the grid spacing at $T = -100M$ is 0.01, 0.0057, 0.0031 respectively at the 3 different resolutions used. I.e. very similar to the results for Schwarzschild in isotropic coordinates.

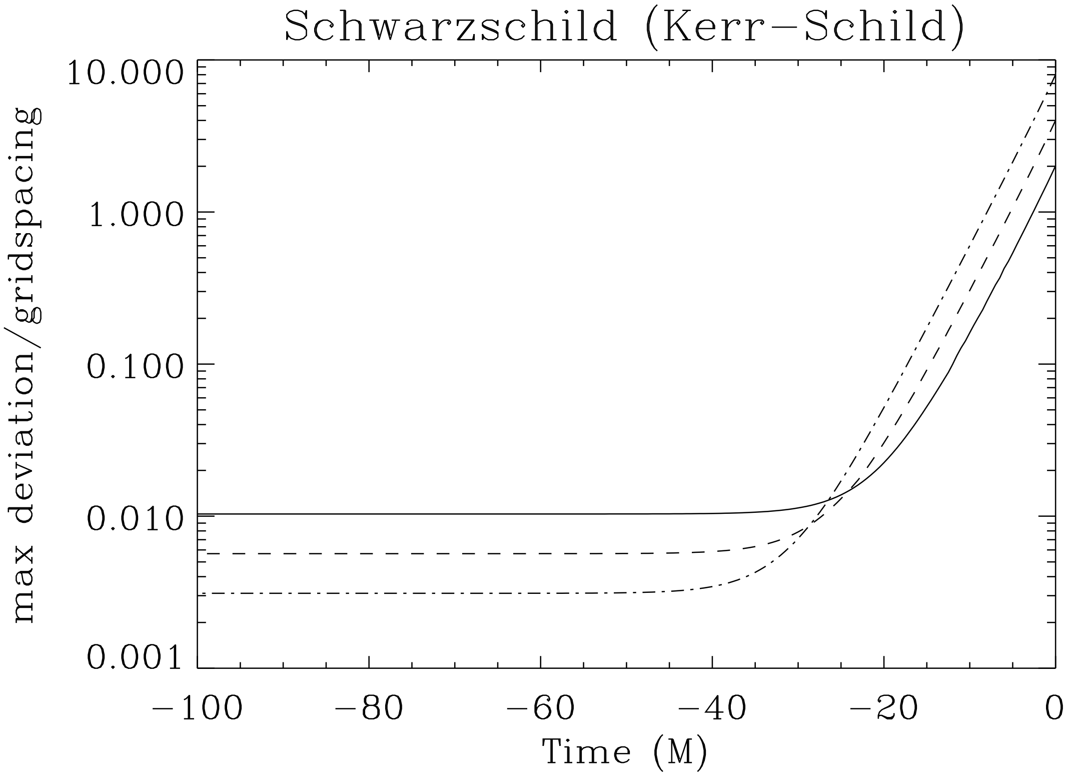

Figure 2. The maximum deviation of the surface from the analytic EH divided by the gridspacing for a Schwarzschild black hole of mass $M = 1$ in Kerr-Schild coordinates as function of time. The solid line is $\Delta = 0.2M$, the dashed line is $\Delta = 0.1M$ and the dash-dot line is $\Delta = 0.05M$.

5.3. Rotating black hole in Kerr-Schild coordinates

The third test uses the metric for a rotating black hole in Kerr-Schild coordinates. In these coordinates the EH is an ellipsoid with the following equation

$$d \equiv \frac{x^2 + y^2}{r_+^2 + a^2} + \frac{z^2}{r_+^2} - 1 = 0, \tag{10}$$

where $r_+ = M + \sqrt{M^2 - a^2}$, M is the mass and $a = J/M$ is the angular momentum per unit mass. For points not located on the EH the deviation, d, defined in equation (10) can be used as a measure of the error. However it will not be a direct measure of the distance from the surface to the EH. Usually it will be somewhat larger than the distance.

I performed runs at four different resolutions $\Delta = 0.2M, 0.1M, 0.05M, 0.025M$ for $M = 1$ and $a = 0.8$ with an initial radius for the null surface equal to $r_0 = 2.0$ in all cases. In figure 3 I plot the deviation as defined in equation (10) divided by the gridspacing as a function of time in a logarithmic plot. At all resolutions there is a nice exponential convergence until the finite difference solution is reached with a numerical e-folding time of 5.18. The deviation, d, divided by the grid spacing at $T = -100M$

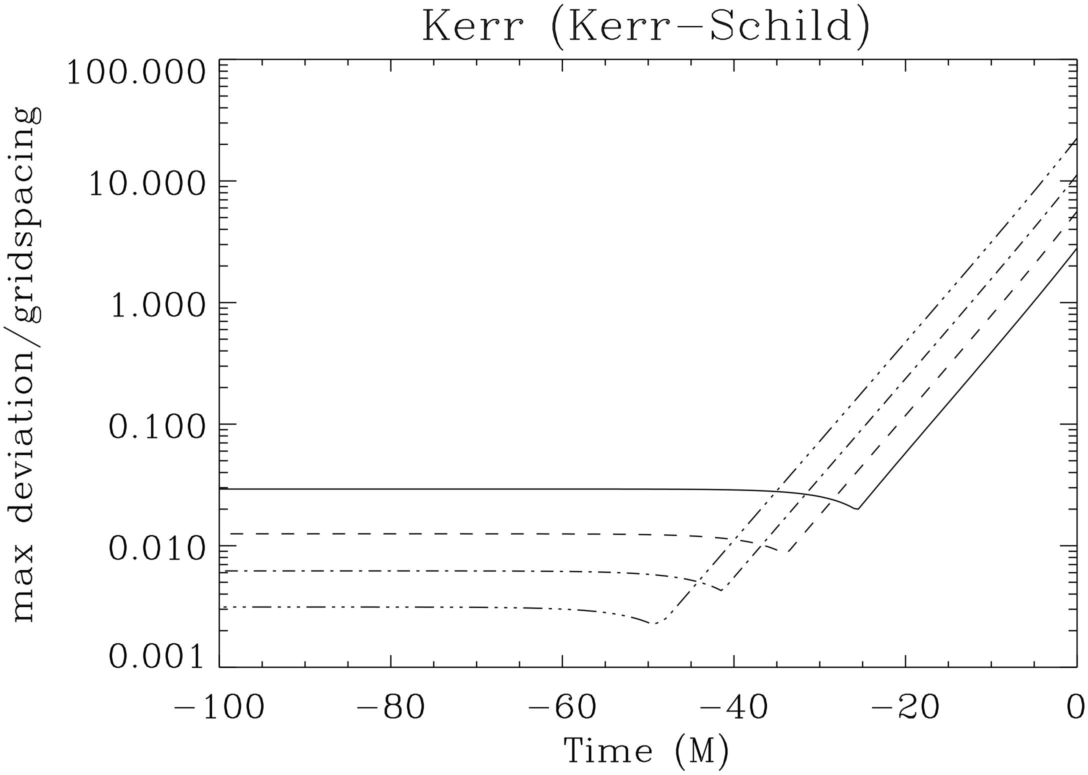

Figure 3. The maximum deviation, as defined in equation (10), divided by the gridspacing for a Kerr black hole of mass $M = 1$ and $a = 0.8$ in Kerr-Schild coordinates as function of time. The solid line is $\Delta = 0.2M$, the dashed line is $\Delta = 0.1M$, the dash-dot line is $\Delta = 0.05M$ and the dash-triple-dot line is $\Delta = 0.025M$.

goes down at higher resolution. For the four resolutions it is $0.029, 0.013, 0.0062, 0.0031$ respectively, showing perfect second order convergence.

6. Tests using numerical data

In this section I will present results from tests based on metric data from highly dynamic spacetimes evolved numerically with Cactus. The exact location of the EH is not known in these numerical spacetimes, but I compare to other published results to the extent possible. At the same time it will be a test of the robustness of the code and how well it can handle changes of topology in multiple black hole spacetimes.

6.1. Misner data with $\mu = 2.2$

In [22] initial data describing two black holes, initially at rest, was presented. The initial separation between the two black holes is described by a parameter μ. These types of initial data have been extensively studied in the literature and especially the EH for these data was studied using numerical data from axisymmetric 2D codes and from 3D codes in [3], [4] and [23].

The spacetime was evolved using the BSSN formulation of the Einstein equations developed in [24] and [25] and implemented in Cactus in [26]. In order to be able to compare with the results in [3] I used maximal slicing. The run was done at fairly low resolution of $\Delta = 0.128M$ in order to be performed with a modest amount of output on a workstation. With the recent development of improved shift conditions in [1], it turned out to be advantageous to use the hyperbolic version of the gamma freezing shift. In this way the slice stretching was controlled, the expansion of the horizon in coordinate space was strongly reduced and it was possible to evolve for a very long time. In the present case, the evolution was halted at $T = 70M$, since this is long enough to track the EH accurately for the first $50M$ of the evolution.

At $T = 70M$ the AH was found in the numerical data and it turned out to be nearly spherical with a coordinate radius of $r_{AH} = 2.84M$ (the ratio of the equatorial to the polar circumference was $C_{eq}/C_{pol} = 1.00074$). Two different runs with the EH finder were therefore started at $T = 70M$; one run where the initial surface described by $f = 0$ was a sphere of radius $r_I = 2.5M$ completely contained within the AH and another run with an initial sphere of radius $r_O = r_I + 0.5M = 3.0M$ which seemed to be a safe guess for a surface completely outside of the EH. This was confirmed by the fact that initially the inner surface was expanding while the outer surface was contracting when the surfaces were evolved backwards in time.

Both of these surfaces were evolved successfully backwards in time, through the change of topology all the way to the initial data slice. The change of topology occurred at around $T \approx 2.75M$.

In [4] it can be seen from figure 11 that the topology changes between $T = 2M$ and $T = 3.3M$. However, it turns out that a more precise transition time is $T \approx 3.2M$ [27], which is somewhat later than the transition time $T \approx 2.75M$ found above. Since in both cases maximal slicing was used, the difference must come from a difference in the initial slicing. In [4] the Čadež lapse profile, which is zero at the throats, was used initially, while in the current work the initial lapse was one. Therefore in this case the evolution proceeds somewhat faster until the lapse collapses, compared to the case with the lapse initially collapsed at the throats, resulting in a shorter time for the change of topology. It is not currently possible to use the Čadež initial lapse profile in Cactus, so a direct comparison is unfortunately not possible. However, the results are consistent.

In the left plot in figure 4 I show the total irreducible mass of the horizons for the Misner $\mu = 2.2$ spacetime as a function of time for the two different choices for the initial surfaces mentioned previously. The total irreducible mass is defined as

$$M_{ir} = \sqrt{\frac{\sum_{i=1}^{n} A_i}{16\pi}},$$

where n is the number of horizons in the spacetime and A_i is the area of the i'th horizon. As can be seen, even though M_{ir} of the two surfaces are very different at $T = 70M$, they are almost indistinguishable on this plot for $T < 50M$. The fact that the curve crosses the dotted line and the subsequent rise in M_{ir} from about $T = 20M$ to $T = 50M$

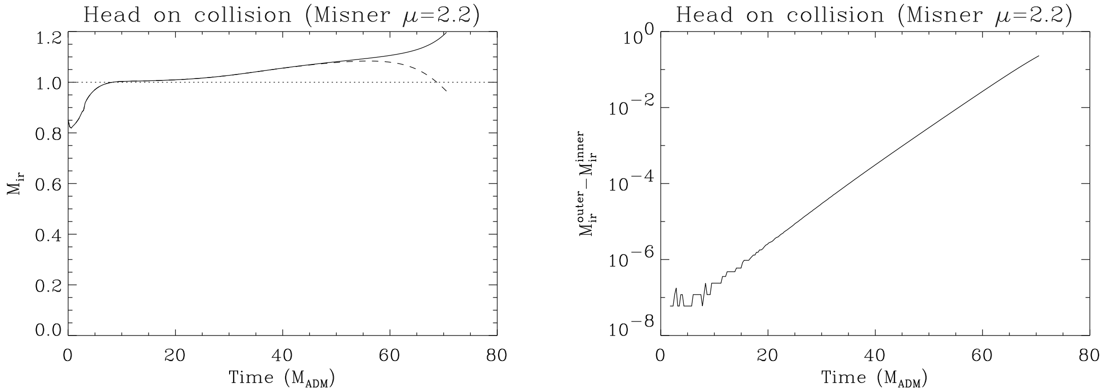
Head on collision (Misner μ=2.2)

Head on collision (Misner μ=2.2)

Figure 4. The plot on the left shows the total irreducible mass of the horizons in the Misner $\mu = 2.2$ spacetime as a function of time. Shown is curves for two different choices of surfaces at $T = 70M$. The solid line is for a sphere with radius $r_O = 3.0M$ and the dashed line is for a sphere with radius $r_I = 2.5M$. The horizontal dotted line denotes the ADM mass of the spacetime The plot on the left shows the difference in mass of the two surfaces.

are due to the lack of accuracy of the underlying numerical data. The run was done at comparatively low resolution and there are also reflections from the outer boundary. The initial dip in M_{ir} must be due to the low resolution (initially the horizons are approximately $0.25M$ in radius) but as the horizons expand in coordinates they become better resolved and the areas, and therefore M_{ir}, correspondingly more accurate.

The right plot in figure 4 shows the expected exponential convergence in the difference in M_{ir} for the same two choices of the initial surfaces. Looking closer it can be seen that the convergence is in fact slightly better than exponential, but since the horizon mass is growing slightly with time, this is to be expected. The noise in the beginning, at $T < 10M$, is a lot smaller than the truncation error in either the interpolation and the finite differencing used in obtaining the area.

6.2. "Head on" collision of 3 black holes

Since the Misner data is axisymmetric, the robustness of the code towards non-symmetric data was not really tested in the previous section. Therefore I performed a numerical run with a three black hole spacetime. To keep things simple I used Brill-Lindquist initial data [28] that contains no linear and angular momentum. However, I placed the three black hole punctures on a plane in coordinate space that was tilted with respect to the coordinate axis and with slightly different coordinate distances between the black holes. The masses were chosen to be equal $M_1 = M_2 = M_3 = 0.5$ giving a system with an ADM mass of $M_{ADM} = 1.5$§. The three position vectors were $\mathbf{r}_1 = (1.2, 1.4, -0.8)$, $\mathbf{r}_2 = (-1.6, -0.6, -0.8)$ and $\mathbf{r}_3 = (0.4, -0.8, 1.6)$ giving a system

§ For Brill-Lindquist data the ADM mass is just the sum of the individual black hole mass parameters, while the bare masses are different from the mass parameters.

with the center of mass at the origin. The coordinate distances were thus $d_{12} \approx 3.44$, $d_{13} \approx 3.35$ and $d_{23} \approx 3.13$.

The spacetime was evolved similarly to the Misner spacetime in the previous section, though a hyperbolic K-freezing slicing was used instead of maximal slicing, simply because it is much faster. I used a fairly low resolution of $\Delta = 0.2$, since the purpose was not to test the accuracy but rather the robustness of the code. The run could then be performed on a workstation with a moderate amount of disk requirements. Using the hyperbolic gamma freezing shift it was possible to evolve until $T = 40 = 26.7M_{ADM}$ at which time I stopped the evolution. The run could have continued a bit longer but the Hamiltonian constraint was starting to grow significantly‖ and I estimated that the evolution time was long enough to locate the EH accurately enough for the initial $10M_{ADM}$ of evolution.

At about $T = 10 = 6.7M_{ADM}$ a common AH appeared and at $T = 40 = 26.7M_{ADM}$ it had evolved into an approximately spherical shape with a coordinate radius of $r_{AH} = 3.6$. The deviations from sphericity was less than 1%. Therefore it was safe to assume that a sphere of radius $r_I = 3.5$ was completely contained within the EH at $T = 40 = 26.7M_{ADM}$ and this was chosen as the inner initial guess for the EH, while the outer initial guess was chosen to be a sphere of radius $r_O = 3.7$.

In figure 5 four frames showing the interesting part of the evolution of the EH can be seen. Frame (a) shows 3 separated horizons at $T = 2.067M_{ADM}$. The individual horizons are clearly distorted and it can be seen that they "feel" each other. Frame (b) shows that at $T = 2.1M_{ADM}$ two of the horizons has merged while the third is still clearly well separated. This has changed at $T = 2.267M_{ADM}$ shown in frame (c) where the final horizon has merged with the two other. In frame (d) the horizon is shown at $T = 2.667M_{ADM}$, where it has started to increase in thickness. At later times the EH becomes more and more spherical.

The spatial and time resolution in the metric data is not high enough to find instances of toroidal EHs as predicted in [29], since these are generally short lived and have sharp features. However, looking at frames (b) and (c), it does not take much imagination to envision that a toroidal EH could appear for a short time, given higher spatial and time resolution.

The plots in figure 6 shows the total irreducible mass of the horizons, M_{ir} in the spacetime as a function of time for the two different choices of initial surfaces at $T = 26.7M_{ADM}$. In these plots I had to exclude a few points corresponding to times where the shape of the horizon is so distorted that describing it with $r(\theta, \phi)$ around a suitably chosen center is impossible (see e.g. frame (b) in figure 5). Again M_{ir} goes beyond the limiting value set by the ADM mass of the system, but in this case the resolution is even lower than in the Misner case so this is not surprising. The convergence of the two surfaces are also here nicely exponential, though the surfaces do not get as close together as in the Misner case due to the shorter evolution time.

‖ The growth of the Hamiltonian constraint was contained mostly within the apparent horizon and was rather small in the exterior.

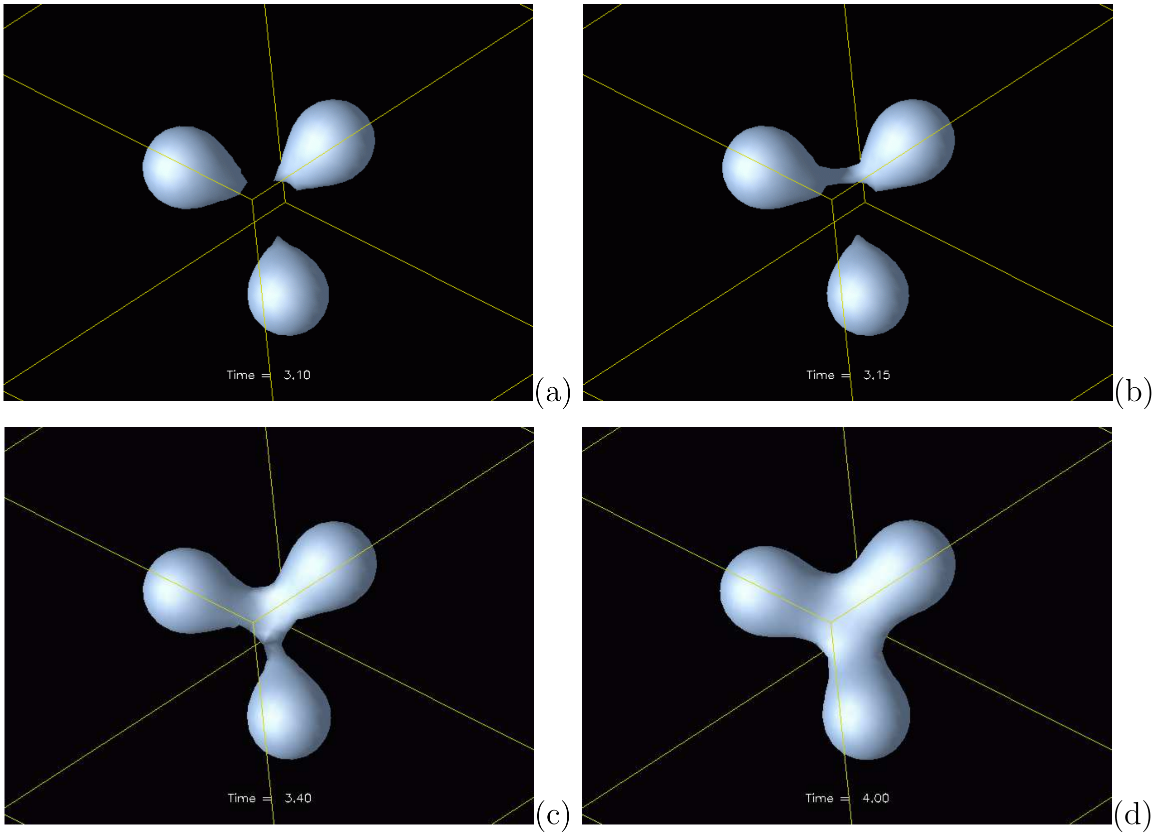

Figure 5. Four frames of the evolution of the EH in a 3 black hole spacetime (Brill-Lindquist). Frame (a) is at $T = 3.1 = 2.067 M_{ADM}$, frame (b) is at $T = 3.15 = 2.1 M_{ADM}$, Frame (c) is at $T = 3.4 = 2.267 M_{ADM}$ and frame (d) is at $T = 4.0 = 2.667 M_{ADM}$. The straight lines in the plot, shows the bounding box of the numerical data. The outer boundary was much further out in the the evolution of the spacetime.

7. Discussion

The EH finder presented here is a very general and accurate method of locating and tracking EHs. It works both with analytic and numerical metric data and on spacetimes with single or multiple black holes and can handle changes of topology (and even though it has not been demonstrated here, it should be able to handle toroidal EHs). For analytic and stationary spacetimes the horizon can typically be located to within a small fraction of a cell size (on the order of $1/10\Delta$– $1/100\Delta$) at typical resolutions and the code shows second order convergence with the grid resolution.

The currently implemented analysis tools are restricted to calculating the area, centroid and polar and equatorial circumferences[¶] for all the surfaces present in the data as long as the surfaces can be represented in spherical coordinates as $r(\theta, \phi)$ around a point inside the surface. As shown in figure 5 this is not always possible, so a more general area integration routine is under consideration.

[¶] The circumferences only makes sense in spacetimes with sufficient symmetries.

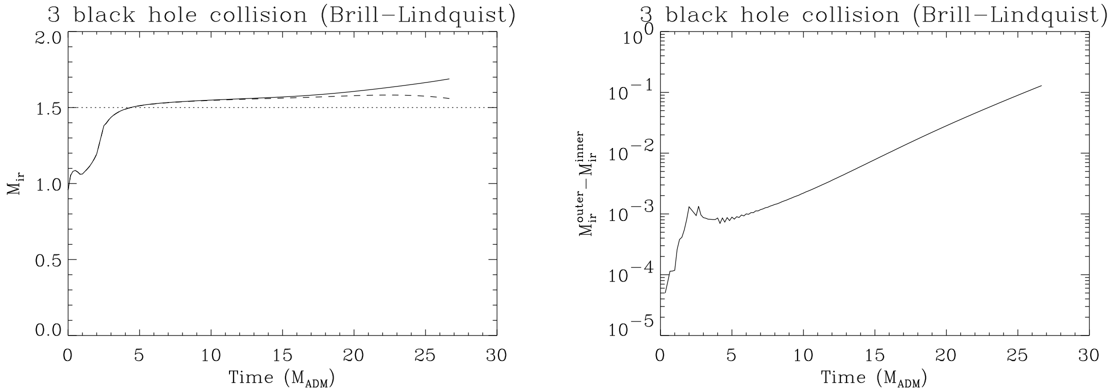

Figure 6. The plot on the left shows M_{ir} in the 3 black hole spacetime as a function of time. Shown is curves for two different choices of surfaces at $T = 27.7M_{ADM}$. The solid line is for a sphere with coordinate radius $r_O = 3.7$ and the dashed line is for a sphere with radius $r_I = 3.5$. The horizontal dotted line indicates the ADM mass, $M_{ADM} = 1.5$, of the system. The plot on the left shows the difference in M_{ir} for the two surfaces.

The robustness of the code was demonstrated by finding and tracking the EH of a three black hole spacetime with no symmetries through two changes of topology.

Analysis tools for calculating the Gaussian curvature of the horizon and for tracking a congruence of individual generators of the horizon surface have been shown in [5] to be useful for extracting physical information from highly dynamic spacetimes. With a congruence of horizon generators, it is possible to construct the membrane paradigm quantities [30] and thus to study the shear and expansion of the horizon in detail. It should be possible to track individual generators along with the horizon surface using the information contained in the level set function. I am currently investigating a way to implement this powerful analysis tool.

The prediction of the generic formation of toroidal EHs (at least for a short while) in non-symmetric spacetimes [29] is interesting. I believe that high resolution is required to see this numerically, but it might be within the realm of possibility with this code.

This EH finder will be applied to a large number of different black hole spacetimes that can be evolved long enough to reach an almost stationary state.

Acknowledgments

During the final phase of writing this paper, two other papers about EH finding methods [31, 32] appeared on GR-QC.

Tests of the code have been performed on the Hitachi SR8000-F1 at the Leibniz-Rechenzentrum (LRZ), the IBM SP RS/6000 at the National Energy Research Scientific Computing Center (NERSC), the IA-32 Linux cluser at the National Center for Supercomputing Applications (NCSA), various workstations at the Albert-Einstein-Institut (AEI), my laptop and on the new Linux cluster (Peyote) at the AEI. I would like to thank Ed Seidel, Sascha Husa, Denis Pollney, Fransisco Guzman, Ian Hawke, Jonathan Thornburg and Jeffrey Winicour for helpful discussions. On the practical side I would like to thank Ian Hawke for implementing the MoL thorn in Cactus making it easy to write an evolution code, Jonathan Thornburg for implementing the new interpolator in Cactus that can return both the interpolated function and its derivatives at the same time and Thomas Radke for helping me with the IO aspects of the code. I would also like to thank the Tapir group at Caltech for useful comments after my talk during my visit in February.

This work was supported by the EU Programme 'Improving the Human Research Potential and the Socio-Economic Knowledge Base' (Research Training Network Contract HPRN-CT-2000-00137).

Appendix A. Level set evolution in Kerr-Schild coordinates

In this appendix I will show that, for a non-rotating black hole in Kerr-Schild coordinates, an analytic solution to the evolution equation for the level set function f only exist for a limited time when evolving backwards in time. I will only consider the spherically symmetric case $f = f(r)$. With the metric given by equation (9) the relevant components of the contravariant metric is

$$g^{tt} = -\left(1 + \frac{2M}{r}\right), g^{tr} = \frac{2M}{r}, g^{rr} = 1 - \frac{2M}{r},$$

and the evolution equation for f becomes

$$\frac{\partial f}{\partial t} = \frac{2M - r}{2M + r}\frac{\partial f}{\partial r}. \tag{A.1}$$

For $r = 2M$ this equation has the trivial solution

$$f(t, r = 2M) = c,$$

where c is a constant depending only on the initial value of f at $r = 2M$. For $r \neq 2M$ this equation has the general solution

$$f(t, r) = h(u(t, r)) = h(t - r - 4M \ln|2M - r|), \tag{A.2}$$

where $u(t, r) = t - r - 4M \ln|2M - r|$. I now limit myself to $r < 2M$. At $t = 0$ the following relation between $u(0, r) = u_0(r)$ and r can be found

$$u(0, r) = u_0(r) = -r - 4M \ln(2M - r).$$

The function $u_0(r)$ has the properties that $\lim_{r\to-\infty} = \infty$ and $\lim_{r\to 2M^-} = \infty$ and it has exactly one minimum in between at $r = -2M$ where the value is $u_0(-2M) = 2M - 4M \ln(4M)$. The range of $u(0, r) = u_0(r)$ is therefore the unbounded interval $[2M - 4M \ln(4M), \infty)$, which again is the domain of the $h(u)$. The function, $h(u)$, does not change in time, so in order for the solution, $f(t, r)$ to exist, $u(t, r)$ must satisfy $u(t, r) \geq 2M - 4M \ln(4M)$. From this it can be seen that a solution exists only at $r = 0$ for

$$t \geq 2M - 4M \ln 2 \approx -0.77259M.$$

There is no limit to the existence of a solution when evolving forward in time. In the solution, the problem shows up as the development of infinite derivatives, $\partial f(t,r)/\partial t$ and $\partial f(t,r)/\partial r$, at $r=0$ in a finite time. Excising a region around $r=0$ does not help, as the point of infinite gradient moves outward and will reach the boundary of the excision region in a finite time. The time for the development of infinite gradients is independent of the initial shape of $f(0,r)$ and are purely a property of the metric. A non rotating black hole in isotropic coordinates do not have the same property. In that case it takes infinite time to develop infinite gradients.

Appendix B. Second order upwinded derivatives

Define a_l and a_r as the second order one sided derivatives of f in the x-direction as

$$\begin{aligned} a_l &= \frac{3f_{i,j,k} - 4f_{i-1,j,k} + f_{i-2,j,k}}{2\Delta}, \\ a_r &= \frac{-3f_{i,j,k} + 4f_{i+1,j,k} - f_{i+2,j,k}}{2\Delta}. \end{aligned}$$

Then define the negative and positive parts of a_l and a_r as

$$\begin{aligned} a_l^- &= \frac{a_l - \|a_l\|}{2}, \; a_l^+ = \frac{a_l + \|a_l\|}{2}, \\ a_r^- &= \frac{a_r - \|a_r\|}{2}, \; a_r^+ = \frac{a_r + \|a_r\|}{2}. \end{aligned}$$

If $f_i \geq 0$ then

$$\frac{\partial f}{\partial x} \approx \begin{cases} a_l^+ & \text{if} \quad a_l^+ > -a_r^- \\ a_r^- & \text{otherwise.} \end{cases}$$

If $f_i < 0$ then

$$\frac{\partial f}{\partial x} \approx \begin{cases} a_l^- & \text{if} \quad -a_l^- > a_r^+ \\ a_r^+ & \text{otherwise.} \end{cases}$$

Derivatives with respect to y and z are approximated by corresponding equations. This method of upwinding derivatives is a generalization of the first order method presented in [18] to second order derivatives. The first order method is shown to be a consistent monotone scheme for the equation under consideration in [18]. The above second order generalization is not guaranteed to be a consistent monotone scheme for the equations considered here, but it works nicely in practice.

References

[1] M. Alcubierre *et al.*, Phys. Rev. D **67**, 084023 (2003).
[2] S. Hughes *et al.*, Phys. Rev. D **49**, 4004 (1994).
[3] P. Anninos *et al.*, Phys. Rev. Lett. **74**, 630 (1995).
[4] J. Libson *et al.*, Phys. Rev. D **53**, 4335 (1996).
[5] J. Massó, E. Seidel, W.-M. Suen, and P. Walker, Phys. Rev. D **59**, 064015 (1999).
[6] T. Nakamura, Y. Kojima, and K. Oohara, Phys. Lett. **106A**, 235 (1984).
[7] K. P. Tod, Class. Quantum Grav. **8**, L115 (1991).

[8] A. J. Kemball and N. T. Bishop, Class. Quantum Grav. **8**, 1361 (1991).

[9] T. W. Baumgarte *et al.*, Phys. Rev. D **54**, 4849 (1996).

[10] J. Thornburg, Phys. Rev. D **54**, 4899 (1996).

[11] C. Gundlach, Phys. Rev. D **57**, 863 (1998), gr-qc/9707050.

[12] P. Anninos *et al.*, Phys. Rev. D **58**, 024003 (1998).

[13] M. Alcubierre *et al.*, Class. Quantum Grav. **17**, 2159 (2000).

[14] D. M. Shoemaker, M. F. Huq, and R. A. Matzner, Phys. Rev. D **62**, 124005 (12 pages) (2000).

[15] M. F. Huq, M. W. Choptuik, and R. A. Matzner, Phys. Rev. D **66**, 084024 (20002), gr-qc/0002076.

[16] E. Schnetter, (2002), gr-qc/0206003.

[17] J. Thornburg, (2003), in preparation.

[18] M. Sussman, P. Smereka, and S. Osher, J. Comp. Phys. **114**, 146 (1994).

[19] G. Allen, T. Goodale, and E. Seidel, in *7th Symposium on the Frontiers of Massively Parallel Computation-Frontiers 99* (IEEE, New York, 1999).

[20] T. Goodale *et al.*, in *Vector and Parallel Processing - VECPAR'2002, 5th International Conference, Lecture Notes in Computer Science* (Springer, Berlin, 2003).

[21] T. Goodale, (2003), in preparation.

[22] C. Misner, Phys. Rev. D **118**, 1110 (1960).

[23] P. Anninos, J. Massó, E. Seidel, and W.-M. Suen, Physics World **9**, 43 (1996).

[24] M. Shibata and T. Nakamura, Phys. Rev. D **52**, 5428 (1995).

[25] T. W. Baumgarte and S. L. Shapiro, Physical Review D **59**, 024007 (1999).

[26] M. Alcubierre, B. Brügmann, M. Miller, and W.-M. Suen, Phys. Rev. D **60**, 064017 (1999).

[27] E. Seidel, private communication.

[28] D. Brill and R. Lindquist, Phys. Rev. **131**, 471 (1963).

[29] S. Husa and J. Winicour, Physical Review D **60**, 084019 (1999).

[30] *Black Holes: The Membrane Paradigm*, edited by K. S. Thorne, R. H. Price, and D. A. Macdonald (Yale University Press, London, 1986).

[31] S. A. Caveny, M. Anderson, and R. A. Matzner, (2003), preprint gr-qc/0303099.

[32] S. A. Caveny and R. A. Matzner, (2003), preprint gr-qc/0303109.